

Flow-induced deformation of kirigami sheets

Tom Marzin , Kerian Le Hay, Emmanuel de Langre, and Sophie Ramanarivo
LadHyX, CNRS, Ecole Polytechnique, Institut Polytechnique de Paris, 91120 Palaiseau, France



(Received 26 October 2021; accepted 2 February 2022; published 22 February 2022)

We investigate the deformation in a uniform water flow of thin sheets perforated with parallel cuts. Through combined experiments and theory, we show that deployment is governed by the competition between fluid forces and sheet stretchability, which is prescribed by the cut pattern. Importantly, fluid loading is modulated by the local three-dimensional geometry of pores that open upon stretching. This mesostructure offers a lever to influence macroscopic morphing, notably leading here to asymmetric deformations of symmetric planar sheets. It brings to the fore the kirigami cutting technique as a promising framework for the design of flow-responsive components.

DOI: [10.1103/PhysRevFluids.7.023906](https://doi.org/10.1103/PhysRevFluids.7.023906)

I. INTRODUCTION

Compliant components are rapidly emerging as a lightweight and versatile alternative to rigid ones in the design of structures exposed to winds and water currents. Flexibility confers resilience in fluctuating fluid environments [1,2], and flow-induced deformation can fulfill functional roles such as enhancing aerodynamic performances [3–5], energy harvesting from currents [6,7], or passive flow control for soft valves [8,9]. Current implementations show promises for flow-responsive components, but applications are still limited by the deformations we are able to achieve. To date, significant experimental and modeling efforts focused on the interaction with fluids of flexible slender structures such as beams or thin-walled plates and shells, which are particularly prone to deformation [1,2,10–13]. Shape transformation is then dictated by the balance between fluid loading and elastic restoring forces, originating for the most part from bending owing to small thicknesses. Those structures thus primarily undergo inextensional deformations, which place restrictions on accessible shapes.

An emergent technique to program shape shifting is to embed a network of cuts into surfaces, which is the principle of kirigami. It allows an initially flat sheet to transform into arbitrary three-dimensional geometries, through local in-plane extension enabled by slits [14–16]. It also produces highly stretchable structures, with mechanical properties primarily prescribed by the arrangement of cuts [17–21]. This engineered elasticity and morphing prompted the use of the kirigami technique for applications as diverse as stretchable and conformable robotics skins, electronics, optoelectronics, sensors, and actuators [22–28]. With an eye towards designing stimuli-responsive materials, previous work probed the kirigami mechanical response to external cues, from uniaxial traction [16] to distributed loading such as gravity or pneumatic actuation [29,30]. However, their behavior in a fluid flow environment remains fairly unexplored. The latter entails distinctive couplings between the deformable structure and the flow causing its deformation, which translate into shape-dependent distributed loading.

Here, we study the impact of cuts on the response of sheets to flow and how the kirigami technique can be leveraged in flow-induced shape transformations. We focus on a generic kirigami pattern of parallel slits [17,19,21–23,31], which enables the sheet to extend through out-of-plane buckling of the remaining uncut material. We investigate its deformation in a uniform flow through

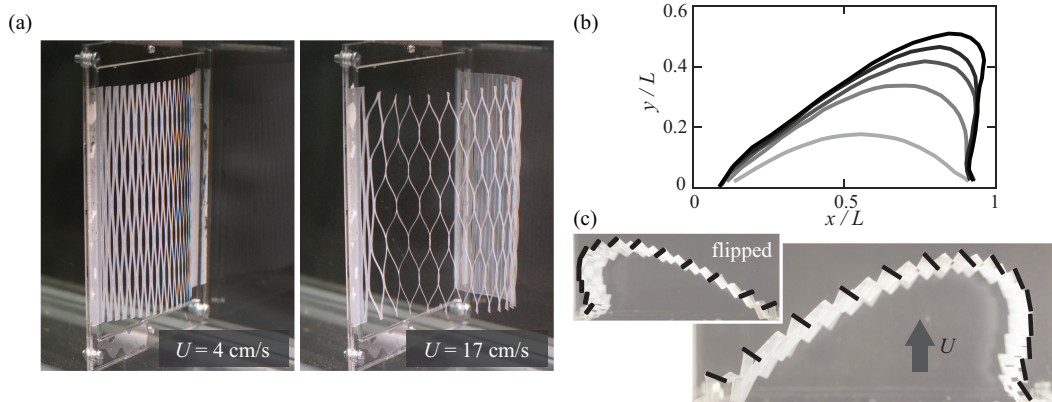


FIG. 1. Flow-induced deformation of a kirigami sheet. (a) Deployment in a water crossflow. (b) Typical shape profiles extracted from top-view pictures of the structure of length L , when increasing the flow speed $U = [4, 8, 13, 17, 21]$ cm/s (denoted by the grayscale). (c) The tilting of buckled cut units (outlined in black) induces tangential fluid forces, resulting in asymmetric profiles prescribed by the buckling direction (reversed in the inset)

combined experiments and theoretical modeling. A salient feature is that stretching occurs through a significant opening up of the material, which allows fluid to go through it. The system thus acts as a poroelastic one, with strong couplings between the elastic deformation of the porous surface and the fluid flow. Note that here, “pore” designates the small-scale openings in the kirigami structure. We show that the cut pattern allows us to tailor the magnitude of the sheet expansion, by providing a simple and robust way to tune mechanical properties. But importantly, material buckling produces pores with an evolving three-dimensional morphology, which affects the magnitude and directionality of local fluid forces. It notably leads here to the asymmetric morphing of symmetrically cut sheets. While the three-dimensional (3D) texturing of stretched kirigami sheets has previously been envisioned for flow control [32,33], here, the pore shape changes with macroscopic deformation, thus intricately coupling local interactions with flows and global morphing. Those couplings open up interesting prospects for programmable flow-driven shape transformations.

II. EXPERIMENTAL SETUP AND RESULTS

A. Experimental approach

Kirigami specimens are fabricated through laser cutting of a $100\text{-}\mu\text{m}$ -thick sheet of Mylar. We present here key features of the experiments and additional details are available as Supplemental Material [34]. The flat surface is clamped at its two extremities to a frame that is adjusted to the 15×15 cm section of a closed water tunnel [Fig. 1(a)]. In a typical experiment, the structure is subjected to a uniform crossflow with speed gradually increased within $U \sim 4\text{--}21$ cm/s. As a result, it stretches, opening pores that in turn influence the fluid loading. The deformation is invariant along the sheet height $H = 10.7$ cm, and is captured by a camera placed above the setup. Two-dimensional profiles are extracted and reported in Fig. 1(b), showing the significant expansion of the sheet with flow speed, which tends to slow as porosity increases. In the following, we will use the dimensionless amplitude of that deformation y_{\max}/L (with $L = 12.4$ cm the sheet length) as a simple observable to characterize behaviors. A striking observation is the asymmetry of the profiles, despite the symmetry of the cutting pattern. As will be discussed in more detail later, it arises from the three-dimensional morphology of stretched pores. Upon elongation, the out-of-plane buckling of cut units produces a texture akin to blades [outlined in Fig. 1(c)] that are inclined with respect

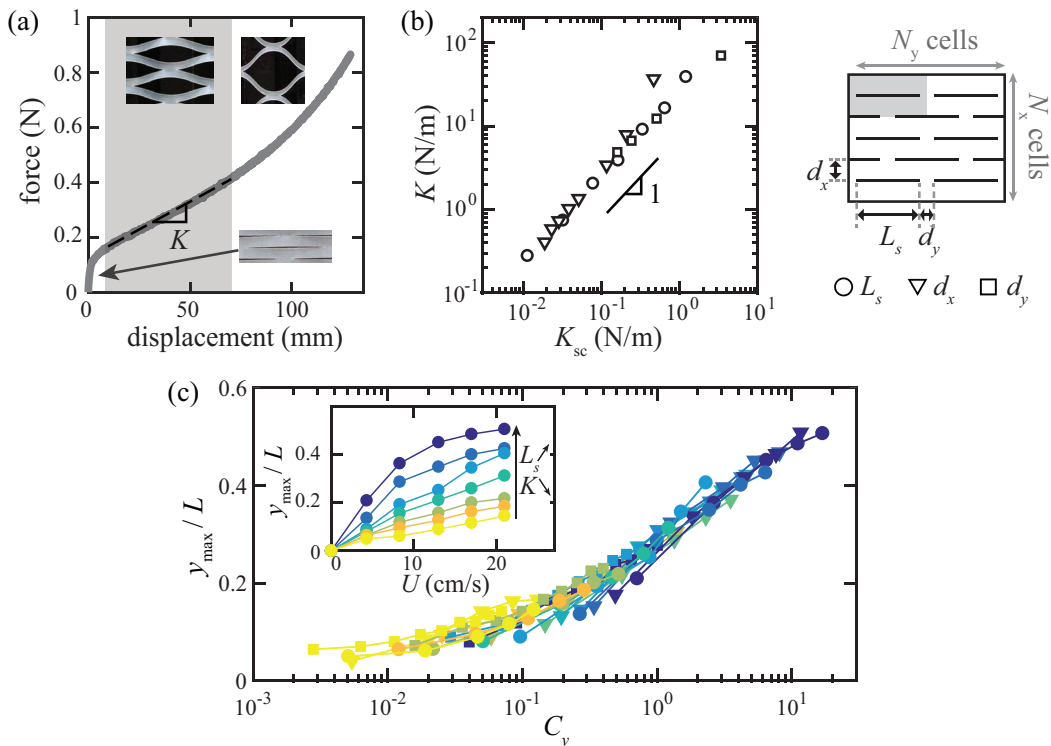


FIG. 2. Fluid-elastic interaction. (a) Typical force-displacement curve for a kirigami sheet. (b) Effective stiffness K measured in the intermediate linear regime [gray zone in (a)], and compared to the predicted scaling K_{sc} [see Eq. (1)]. Cutting parameters (see schematics) are varied within $L_s = 1.7\text{--}4.9$ cm, $d_x = 2\text{--}9$ mm, and $d_y = 2\text{--}18$ mm. (c) Inset: Dimensionless deformation amplitude y_{max}/L as a function of flow speed U , for specimens with increasing slit length L_s . Results replotted as a function of the Cauchy number C_y [see Eq. (2)] for all 19 cut patterns. Color gradients differentiate specimens within each parametric series, denoted by symbols.

to the incoming flow. This symmetry breaking at the pore scale produces sideways fluid forces that orient macroscale deformation.

B. Engineered elasticity

Besides setting the shape of pores, the slit arrangement dictates the mechanical properties of the kirigami sheet, and thus the elastic restoring forces opposing its deformation in the flow. We perform mechanical characterization through uniaxial tensile tests, using an Instron 5865 with a load cell 2525-816, measuring force as a function of extension at a low displacement rate. The typical curve of Fig. 2(a) shows a nonlinear response, coherent with previous characterizations [19,21,31]. An initial stiff regime gives way to a significantly softer one, due to a transition from in-plane to out-of-plane deformation. The kirigami sheet then finally hardens as it further expands, with deformation focusing at the extremities of the cuts. In experiments, structures primarily deform within the second mechanical regime [gray zone in Fig. 2(a)]—see Supplemental Material [34]. While it is not entirely the case for the unstretched portion of the sheet in Fig. 1(c), its alignment with the incoming flow tends to reduce its contribution to fluid-elastic interactions. The second regime features a linear force-displacement relationship that can be characterized by an effective in-plane stiffness K . As discussed in Refs. [17,19,21], this K can be varied through the cutting

pattern, namely the following parameters: L_s the slit length, and d_x and d_y the intercut spacings [see the schematics of Fig. 2(c)]. The cuts delineate slender beams that can be viewed as a collection of springs assembled in series and in parallel. The stiffness of a beam, as it bends out of plane, is set by its width d_x , length $L_s - d_y$, thickness t , and Young modulus $E = 4 \pm 0.3$ GPa. The combined contribution of all springs produces an effective stiffness for the sheet that scales as

$$K_{sc} = \frac{N_y}{2N_x} \frac{Et^3 d_x}{(L_s - d_y)^3}, \quad (1)$$

with N_x and N_y the numbers of elementary cutting cells repeated vertically and horizontally. Figure 2(b) shows the stiffness K measured across variations in cutting parameters, and compared with the prediction K_{sc} . We obtain a good agreement: K scales as K_{sc} , with a numerical coefficient of 30 consistent with previous studies [17], and set by the shape and boundary conditions of the constitutive beams. This predictable and tunable elasticity provides a valuable lever to influence the deployment of sheets in a flow.

C. Flow-induced deformation

To assess the effect of the slit pattern on the flow-induced deformation, experiments are conducted in the water tunnel for all specimens. The inset of Fig. 2(b) shows the evolution of the deformation amplitude y_{\max}/L with velocity U , for sheets with different slit lengths L_s . All specimens gradually expand, with a growth of y_{\max} that steadily slows with U , reflecting the qualitative trend evidenced in the shape profiles of Fig. 1(b). Deformation is however less pronounced for smaller slits at a given U . This result is rather intuitive given the previous mechanical characterization, showing that reducing L_s produces stiffer sheets. A natural step is then to define a Cauchy number C_y [2,12,35], which compares the fluid loading per unit length $\rho U^2 H$ to the sheet effective stiffness K :

$$C_y = \frac{\rho U^2 H}{K}. \quad (2)$$

In Fig. 2(c), we recast the deformation amplitudes of all specimens as a function of C_y . Data gather onto a single master curve, showing that the behavior of the kirigami sheets in a flow is governed by this elastohydrodynamical number. This collapse also corroborates stiffness K as the relevant mechanical parameter here.

D. Local interaction with flows

While the Cauchy number provides key insight on the amplitude of the deformation, it does not account for its asymmetry. As mentioned earlier, one has to look at the bladelike small-scale structure of the kirigami sheet to understand this feature [see Fig. 1(c)]. Those inclined blades are subjected to both drag and lift forces, which results in a local fluid loading on the sheet that not only has a normal component, but also a transverse one. The latter induces local tension, consistently deflecting the profile to one side. Note that cut units should *a priori* collectively buckle up or down indiscriminately, but our laser cutting fabrication seems to bias towards a preferred tilting orientation. The latter can however be reversed by flipping the specimen upside down in the water tunnel. The sheet then spontaneously deforms into the left-right mirror image [see the inset of Fig. 1(c)].

III. THEORETICAL MODELING

A. Modeling approach

To better understand the intricate interplay between the fluid flow, the poroelastic kirigami sheet, and its evolving mesostructure, we search for a model that captures the macroscopic response. We highlight here its key steps, and complete derivations are provided in the Supplemental Material

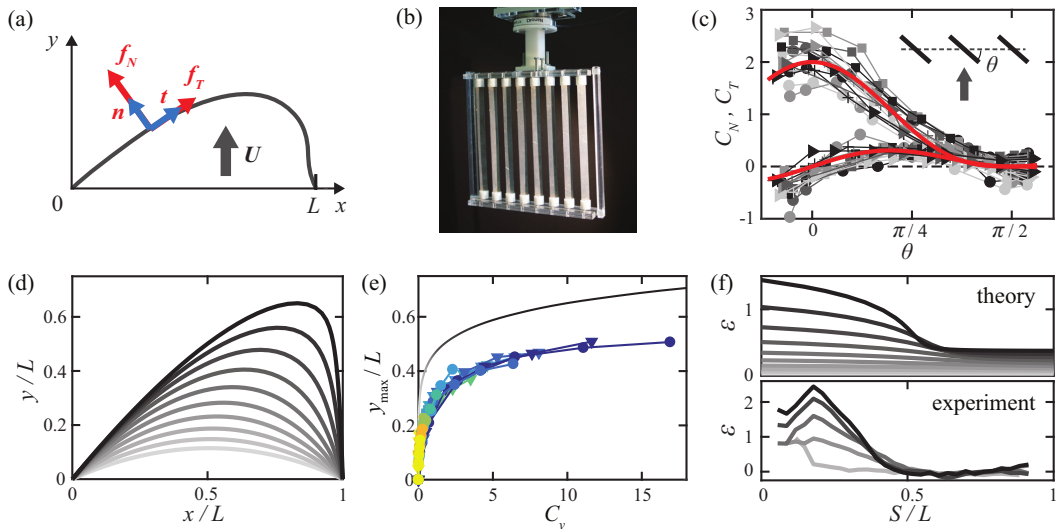


FIG. 3. Theoretical modeling. (a) Model of elastic membrane with distributed fluid loading f_N and f_T . (b) Simplified system of parallel flat blades used to characterize fluid loading experimentally. (c) Fluid force coefficients C_N and C_T for the normal and tangential forces on the array (see main text), as a function of the blades' angle θ (see inset). The grayscale denotes flow speed $U = [7, 10, 14, 17]$ cm/s, and symbols correspond to different center-to-center distances between the 8-mm-width blades: 1.1 (\triangleright), 1.3 ($+$), 1.6 (\square), 2.2 (\circ) cm. (d) Theoretical shape profiles for logarithmically increasing values of C_y in 10^{-3} – 10 (denoted by the grayscale). (e) Corresponding evolution of the dimensionless deformation amplitude y_{\max}/L with C_y , compared to experimental data points [same legend as in Fig. 2(c)]. (f) Top: Evolution with C_y of the local elongation along the curvilinear coordinate S (defined in the unstrained reference configuration). Bottom: The latter is compared to experimental elongations for the typical specimen of Fig. 1(b).

[34]. Inspired by work on porous flexible structures [36–38], we elect not to model each individual pore, and instead opt for a continuous description with net properties. Such modeling describes less accurately the details of the lattice structure and the interstitial flows, but is less computationally costly and proves efficient [36–38]. The kirigami sheet is modeled as an equivalent membrane, with an elastic constitutive law $N = KL\epsilon$ relating the tension force N to the elongation ϵ , in line with results of the mechanical characterization. While we make the approximation of linear elasticity for simplification, note that the force-extension relation can be modified to account for the nonlinearities of Fig. 2(a) (see Supplemental Material [34]). The two-dimensional equilibrium shape of the membrane in a flow is then determined by local force balance,

$$(Nt)' + f_N + f_T = \mathbf{0}, \quad (3)$$

with $'$ denoting the derivative with respect to the curvilinear coordinate S defined in the undeformed state, t the tangent unit vector, and f_N and f_T respectively the normal and tangential components of the external fluid load [see Fig. 3(a)].

B. Fluid loading

The challenge is then to find a simple formulation for the fluid loading, which reflects the influence of the kirigami substructure. To that end, we conduct fluid force measurements on a simplified model system of parallel rigid blades that reproduces the local geometry of stretched kirigami sheets [see Fig. 3(b), and the Supplemental Material [34]]. It is placed perpendicular to the incoming flow and spans most of the cross section of the water tunnel. It is mounted on a six-component force sensor (FT-Nano-43 SI-9-0.125) that measures forces in the normal and

tangential direction, to which we subtract forces on the support frame alone. We vary the orientation of the blades [angle θ in the inset of Fig. 3(c)], their spacing, and the flow velocity. For kirigami specimens, the local Reynolds number—defined with respect to the width of the cut units—varies in the range $\text{Re} = Ud_x/\nu \sim 10\text{--}2000$, with ν the water kinematic viscosity. Experiments on model blades fall within that range. Varying U yields forces consistent with a quadratic velocity dependence, indicating the dominance of fluid inertia over viscosity (see Supplemental Material for additional supporting plots [34]). Changing the spacing between blades reveals blockage effects due to flow obstruction. It shows that the latter can be accounted by an effective velocity $U^* = aU$ as in Ref. [39], with a a numerical factor given by the conservation of mass flow rate through the openings. We thus define effective fluid force coefficients for the normal and tangential net forces on the array F_N and F_T , as $C_{N/T} = F_{N/T}/(1/2\rho AU^{*2})$, with A the cumulated surface area of blades. Figure 3(c) shows their evolution with angle θ , with a collapse of curves across variations in array spacings and flow speed. Following a similar approach as Ref. [40] for forces on inclined slender bodies, we approximate it with $C_N = C_{N0} \cos^3 \theta$ (with $C_{N0} = 2$) and $C_T = C_{T0} \cos^2 \theta \sin \theta$ (with $C_{T0} = 0.8$), which reasonably capture results for this blade arrangement little studied in the literature.

For kirigami sheets, the mesostructure transforms with stretching, as cut units get increasingly tilted and spaced out. Through simple geometrical arguments, a relation can be derived between their rotation angle relative to the sheet centerline and the elongation: $\cos \theta = 1/(1 + \epsilon)$ [22]. Together with previous results from model blades, it provides expressions for the effective fluid force coefficients $C_N(\epsilon)$ and $C_T(\epsilon)$ that are elongation dependent. We further account for the local angle of the membrane relative to the incoming flow by assuming that the latter locally experiences a normal flow with speed $\mathbf{U} \cdot \mathbf{n}$, with \mathbf{n} the normal unit vector [13,37,38]. Note that we consider a uniform incoming velocity \mathbf{U} , which does not account for potential retroaction of the sheet presence on the flow at large scale. We obtain a formulation for fluid forces per unit length,

$$f_{N/T} = \frac{1}{2} C_{N/T}(\epsilon) H[a(\epsilon) \mathbf{U} \cdot \mathbf{n}]^2, \quad (4)$$

with the numerical factor $a(\epsilon)$ reflecting local blockage effects on the flow. Note that the dependence of kirigami porosity (involved in a) on ϵ is independent of the cut geometry—as is also the case for $\theta(\epsilon)$ —so that $f_{N/T}$ is the same function of elongation, irrespective of cutting parameters.

C. Theoretical predictions

Injecting Eq. (4) into Eq. (3) gives the system of equations for the membrane deformation, whose nondimensionalization brings out the same Cauchy number as defined for experiments [Eq. (2)]. We solve the boundary value problem numerically for increasing C_y , using shooting methods. Figure 3(d) shows the resulting shapes, which reproduce qualitatively the asymmetric expansion observed in experiments [see Fig. 1(b)]. A further comparison of the deformation amplitude, reported in Fig. 3(e), shows that the model captures as well the experimental sublinear trend $y_{\max}(C_y)$, although it overestimates the displacement. The agreement is however reasonable given the absence of any fitting parameter and the simplifying assumptions. As shown in Fig. 3(f), the model is also able to predict the local deformation field, with half of the original sheet gradually elongating with C_y , while the other half remains fairly unstretched. Additional computations in the Supplemental Material show that accounting for mechanical nonlinearities does not alter the observed trends, but tends to slightly curtail elongation and amplitude y_{\max} [34]. The stiffer initial response visible in Fig. 2(a) produces an upward shift in tensile forces, resulting in higher resistance to deformation. The present simplified model thus corroborates experiments, and captures the underlying fluid-elastic mechanisms governed by the dimensionless Cauchy number. It also sheds light on the key role of the kirigami substructure in modulating the magnitude and directionality of local fluid forces. The evolution of pore size and shape conditions the velocity of interstitial flows

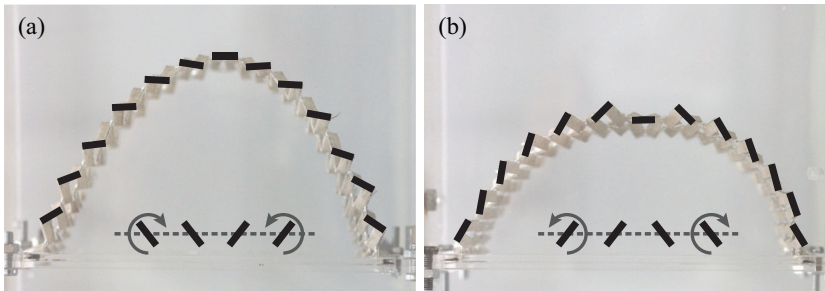


FIG. 4. Programming shape through fluid force polarity. Profiles of sheets designed with dual tilting orientation of cut units, in a flow with speed $U = 21$ cm/s: (a) The left half rotates clockwise while the right one rotates counterclockwise (see inset schematics), and (b) inversely.

and thus the fluid dynamic pressure, as well as the orientation of the surfaces bearing those pressure forces.

IV. CONCLUSION AND OUTLOOK

We have shown that the kirigami cutting principle provides a promising platform to influence the response to flows, through its engineered elasticity and the mesostructure that forms upon stretching. The 3D morphology of this pattern dictates the directionality of local fluid forces, leading here to an unexpected shape asymmetry. Note that while the cut units all buckle in the same direction in the present study, orientation could be varied throughout the sheet to access different deformations. Such deterministic tilting has notably been achieved by introducing notches to guide the buckling [31]. As a proof of concept, we pattern such notches on both sides of a 1.5-mm-thick natural rubber sheet, to achieve opposite tilting orientations in its two halves. When subjected to flow, the structure produces a symmetric deformation that was previously unattainable (see Fig. 4). We further test versatility by reversing the prescribed tilting orientations: Sheets transit from an elongated lobe [Fig. 4(a)] to a rounder profile flattened by fluid forces now pushing outwards [Fig. 4(b)]. Those simple implementations show a potential for programming flow-induced shape transformations.

A natural continuation of our work is reverse engineering, that is, designing perforation templates to find target shapes in a given flow. One can vary spatially the sheet mechanical properties through inhomogeneous cut patterns, but also modulate fluid loading via the geometry of the mesostructure. While the present parallel-slit pattern produces fairly simple shapes, this study could be extended to different kirigami families, producing a variety of 3D-textured surfaces under external load [17,20,28]. Theoretical models as presented here would then play a key role in inverse-design strategies, providing intuition and informing optimization algorithms. Beside programmable morphing, the kirigami principle also opens possibilities for sieve filters or nets with adaptable pore sizes, for selective capture. In this respect, our system bears similarities with the hyperelastic porous membrane of Ref. [41], whose macroscopic deformation impacts the microstructure and subsequent transport properties. Those multiscale fluid-elastic couplings, primarily governed here by the cut pattern, could fuel a prolific branch for fluid-structure interactions and responsive architected materials.

ACKNOWLEDGMENTS

We thank B. Roman and J. Bico for helpful discussions and for the use of their tensile test machine, J. Gouin for early experiments on kirigami with notches, and B. Paixao Peixoto de Vasconcellos for side work on related systems. We acknowledge support from a JCJC Agence Nationale de la Recherche grant (ANR-20-CE30-0009-01) to S.R. and support from the Agence Innovation Défense to T.M.

- [1] S. Alben, M. Shelley, and J. Zhang, Drag reduction through self-similar bending of a flexible body, *Nature (London)* **420**, 479 (2002).
- [2] F. Gosselin, E. de Langre, and B. A. Machado-Almeida, Drag reduction of flexible plates by reconfiguration, *J. Fluid Mech.* **650**, 319 (2010).
- [3] W. Shyy, M. Berg, and D. Ljungqvist, Flapping and flexible wings for biological and micro air vehicles, *Prog. Aerosp. Sci.* **35**, 455 (1999).
- [4] Y. L. Young, Fluid–structure interaction analysis of flexible composite marine propellers, *J. Fluids Struct.* **24**, 799 (2008).
- [5] S. Ramananarivo, R. Godoy-Diana, and B. Thiria, Rather than resonance, flapping wing flyers may play on aerodynamics to improve performance, *Proc. Natl. Acad. Sci. USA* **108**, 5964 (2011).
- [6] S. Michelin and O. Doaré, Energy harvesting efficiency of piezoelectric flags in axial flows, *J. Fluid Mech.* **714**, 489 (2013).
- [7] G. O. Antoine, E. de Langre, and S. Michelin, Optimal energy harvesting from vortex-induced vibrations of cables, *Proc. R. Soc. A* **472**, 20160583 (2016).
- [8] M. Gomez, D. E. Moulton, and D. Vella, Passive Control of Viscous Flow via Elastic Snap-through, *Phys. Rev. Lett.* **119**, 144502 (2017).
- [9] M. Brandenbourger, A. Dangremont, R. Sprik, and C. Coulais, Tunable flow asymmetry and flow rectification with bio-inspired soft leaflets, *Phys. Rev. Fluids* **5**, 084102 (2020).
- [10] E. de Langre, A. Gutierrez, and J. Cossé, On the scaling of drag reduction by reconfiguration in plants, *C. R. Mec.* **340**, 35 (2012).
- [11] L. Schouveiler and A. Boudaoud, The rolling up of sheets in a steady flow, *J. Fluid Mech.* **563**, 71 (2006).
- [12] L. Schouveiler and C. Eloy, Flow-Induced Draping, *Phys. Rev. Lett.* **111**, 064301 (2013).
- [13] P. Buchak, C. Eloy, and P. M. Reis, The Clapping Book: Wind-Driven Oscillations in a Stack of Elastic Sheets, *Phys. Rev. Lett.* **105**, 194301 (2010).
- [14] M. Konaković, K. Crane, B. Deng, S. Bouaziz, D. Piker, and M. Pauly, Beyond developable: computational design and fabrication with auxetic materials, *ACM Trans. Graph.* **35**, 1 (2016).
- [15] S. J. P. Callens and A. A. Zadpoor, From flat sheets to curved geometries: Origami and kirigami approaches, *Mater. Today* **21**, 241 (2018).
- [16] P. Celli, C. McMahan, B. Ramirez, A. Bauhofer, C. Naify, D. Hofmann, B. Audoly, and C. Daraio, Shape-morphing architected sheets with non-periodic cut patterns, *Soft Matter* **14**, 9744 (2018).
- [17] T. C. Shyu, P. F. Damasceno, P. M. Dodd, A. Lamoureux, L. Xu, M. Shlian, M. Shtein, S. C. Glotzer, and N. A. Kotov, A kirigami approach to engineering elasticity in nanocomposites through patterned defects, *Nat. Mater.* **14**, 785 (2015).
- [18] Y. Tang, G. Lin, L. Han, S. Qiu, S. Yang, and J. Yin, Design of hierarchically cut hinges for highly stretchable and reconfigurable metamaterials with enhanced strength, *Adv. Mater.* **27**, 7181 (2015).
- [19] M. Isobe and K. Okumura, Initial rigid response and softening transition of highly stretchable kirigami sheet materials, *Sci. Rep.* **6**, 24758 (2016).
- [20] A. Rafsanjani and K. Bertoldi, Buckling-Induced Kirigami, *Phys. Rev. Lett.* **118**, 084301 (2017).
- [21] D.-G. Hwang and M. D. Bartlett, Tunable mechanical metamaterials through hybrid kirigami structures, *Sci. Rep.* **8**, 3378 (2018).
- [22] A. Lamoureux, K. Lee, M. Shlian, S. R. Forrest, and M. Shtein, Dynamic kirigami structures for integrated solar tracking, *Nat. Mater.* **6**, 8092 (2015).
- [23] M. K. Bles, A. W. Barnard, P. A. Rose, S. P. Roberts, K. L. McGill, P. Y. Huang, A. R. Ruyack, J. W. Kevek, B. Kobrin, D. A. Muller *et al.*, Graphene kirigami, *Nature (London)* **524**, 204 (2015).
- [24] A. Firouzeh and J. Paik, The design and modeling of a novel resistive stretch sensor with tunable sensitivity, *IEEE Sens. J.* **15**, 6390 (2015).
- [25] C. Wu, X. Wang, L. Lin, H. Guo, and Z. L. Wang, Based triboelectric nanogenerators made of stretchable interlocking kirigami patterns, *ACS Nano* **10**, 4652 (2016).
- [26] W. Wang, C. Li, H. Rodrigue, F. Yuan, M.-W. Han, M. Cho, and S-H. Ahn, Kirigami/origami-based soft deployable reflector for optical beam steering, *Adv. Funct. Mater.* **27**, 1604214 (2017).
- [27] M. A. Dias, M. P. McCarron, D. Rayneau-Kirkhope, P. Z. Hanakata, D. K. Campbell, H. S. Park, and D. P. Holmes, Kirigami actuators, *Soft Matter* **13**, 9087 (2017).

- [28] A. Rafsanjani, Y. Zhang, B. Liu, S. M. Rubinstein, and K. Bertoldi, Kirigami skins make a simple soft actuator crawl, *Sci. Robot.* **3**, eaar7555 (2018).
- [29] M. Konaković-Luković, J. Panetta, K. Crane, and M. Pauly, Rapid deployment of curved surfaces via programmable auxetics, *ACM Trans. Graph.* **37**, 1 (2018).
- [30] L. Jin, A. E. Forte, B. Deng, A. Rafsanjani, and K. Bertoldi, Kirigami-inspired inflatables with programmable shapes, *Adv. Mater* **32**, 2001863 (2020).
- [31] Y. Tang, G. Lin, S. Yang, Y. K. Yi, R. D. Kamien, and J. Yin, Programmable kiri-kirigami metamaterials, *Adv. Mater.* **29**, 1604262 (2017).
- [32] L. Gamble, A. Lamoureux, and M. Shtein, Multifunctional composite kirigami skins for aerodynamic control, *Appl. Phys. Lett.* **117**, 254105 (2020).
- [33] J. Li, R. Ran, H. Wang, Y. Wang, Y. Chen, S. Niu, P. E. Arratia, and S. Yang, Aerodynamics-assisted, efficient and scalable *kirigami* fog collectors, *Nat. Commun.* **12**, 5484 (2021).
- [34] See Supplemental Material at <http://link.aps.org/supplemental/10.1103/PhysRevFluids.7.023906> for additional details on experimental methods, the fluid force characterization, the theoretical model, and a discussion on the effect of mechanical nonlinearities.
- [35] E. de Langre, Effects of wind on plants, *Annu. Rev. Fluid Mech.* **40**, 141 (2008).
- [36] H. Tronstad, Nonlinear hydroelastic analysis and design of cable net structures like fishing gear based on the finite element method, Doctor's thesis, Norwegian University of Science and Technology, 2000, <http://resolver.tudelft.nl/uuid:9233229d-f869-4014-b0b2-362df5d0dbca>.
- [37] M. Gutttag, H. H. Karimi, C. Falcón, and P. M. Reis, Aeroelastic deformation of a perforated strip, *Phys. Rev. Fluids* **3**, 014003 (2018).
- [38] Y. Jin, J.-T. Kim, S. Cheng, O. Barry, and L. P. Chamorro, On the distinct drag, reconfiguration and wake of perforated structures, *J. Fluid Mech.* **890**, A1 (2020).
- [39] K. E. G. Wieghardt, On the resistance of screens, *Aeronaut. Q.* **4**, 186 (1953).
- [40] S. F. Hoerner, *Fluid-Dynamic Drag* (Hoerner Fluid Dynamics, 1965).
- [41] R. Song, H. A. Stone, K. H. Jensen, and J. Lee, Pressure-driven flow across a hyperelastic porous membrane, *J. Fluid Mech.* **871**, 742 (2019).